

Superstructure induced by a topological defect in graphitic cones

Katsuyoshi Kobayashi

Department of Physics, Faculty of Science, Ochanomizu University, 2-1-1 Otsuka, Bunkyo-ku, Tokyo 112-8610, Japan

(Received 30 November 1999)

When a pentagon defect is introduced into a graphite sheet, a cone structure is formed. We simulate scanning-tunneling-microscopy (STM) images of the graphitic cone based on density-functional calculations. Simulated STM images show approximately $\sqrt{3} \times \sqrt{3}$ superstructures consisting of ring patterns which reproduce well the petal-like structure observed in experiments. An analysis using the effective-mass theory shows that the superstructures by the topological defects are qualitatively different from those observed often around defects of flat graphite surfaces.

I. INTRODUCTION

Recently carbon nanotubes have been studied extensively using scanning tunneling microscopy (STM), because STM provides simultaneously information about atomic structures and electronic states of sample surfaces with atomic resolution. The correlation between atomic structures and electronic states of nanotubes has been directly verified by STM.^{1,2} In addition, the ends of carbon nanotubes have also attracted much attention,^{3,4} because peculiar electronic states due to topological defects in the caps of nanotubes were theoretically predicted.⁵⁻⁷ Among the topological defects, the pentagon is the most stable⁸ and is frequently observed.

When a pentagon is introduced into a graphite sheet, a cone structure is formed. Graphitic cones have actually been observed in STM (Ref. 9) and transmission electron microscopy,¹⁰ but atomic resolution has not been achieved. Very recently, STM images at conical protuberances of graphitic nanoparticles were observed with atomic resolution.¹¹ The shapes of the protuberances are the same as those of the graphitic cones with a pentagon defect, but the STM images do not show the honeycomb structure of the graphite lattice. Instead, strange structures like petals were observed. The petal structures consist of ring patterns and form approximately $\sqrt{3} \times \sqrt{3}$ superstructures of the graphite lattice.

The aim of this paper is to clarify the origin of the petal structures experimentally observed. For this purpose we simulate STM images of a graphitic cone with a pentagon defect. Electronic states of the graphitic cone are calculated by the density-functional method. Simulated STM images reproduce well the petal-like superstructures, which identifies the observed conical protuberances with graphitic cones.

$\sqrt{3} \times \sqrt{3}$ superstructures have often been observed in STM images of graphite surfaces around defects.¹² These superstructures are interpreted as interference of the Bloch waves of graphite scattered by defects. We apply the effective-mass theory¹³ to the graphitic cone and find that the superstructures induced by topological defects are not the interference of extended Bloch waves but due to peculiar states: the wave functions decay as $r^{-1/5}$ with the distance r from the pentagon defect. This means that the superstructures in graphitic cones are qualitatively different from those in flat graphite surfaces. In Sec. II we show the methods of determining the atomic positions, calculating the electronic

states, and simulating STM images of the graphitic cone. Simulated STM images are presented in Sec. III, where the origin of the superstructure is discussed using the effective-mass theory.

II. METHOD OF CALCULATION

A. Atomic structure

We use a finite-size cluster as a model of graphitic cones. Figure 1 shows a cluster consisting of 500 carbon atoms. There is a pentagon defect at the center of the cluster. Fifty hydrogen atoms are attached to the edge carbon atoms in order to eliminate artificial dangling bonds. We have checked that simulated STM images are almost unchanged by using a cluster consisting of 405 carbon atoms and 45

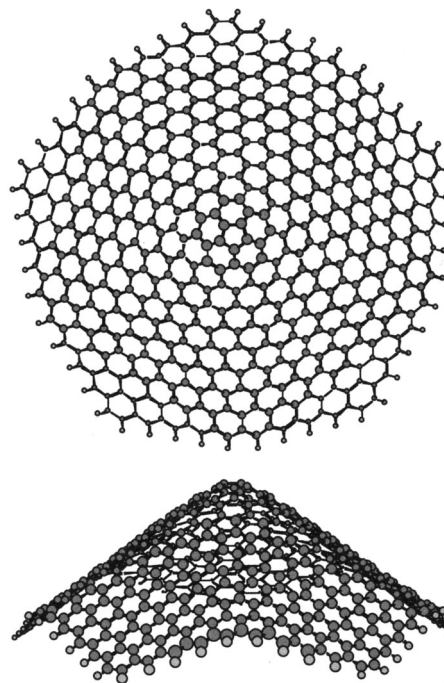


FIG. 1. Atomic structure of the $C_{500}H_{50}$ cluster used in this paper as a model of a graphitic cone. Upper and lower figures show the top and side views, respectively. There is a pentagon at the center of the cluster. Edge carbon atoms are terminated with hydrogen atoms.

hydrogen atoms. We present results calculated for the $C_{50}H_{50}$ cluster throughout this paper.

Positions of the carbon atoms in the cluster are optimized using a refined version of the Tersoff potential,¹⁵ where a torsionlike term is added to the original Tersoff potential. Since the empirical potential is intended for the interaction between carbon atoms, geometry optimization is performed for a cluster consisting of 550 carbon atoms, where the edge hydrogen atoms are replaced with carbon atoms. After optimization, the 50 edge carbon atoms are replaced again with hydrogen atoms. The carbon-hydrogen distance is fixed at 1.1 Å which is the distance in a benzene molecule.

Before optimization the carbon atoms are initially positioned on surfaces of a five-sided pyramid which is made by dividing a graphite sheet into six pieces and sticking together five pieces. Initial carbon-carbon distances are 1.42 Å which is the distance in graphite. By optimization, the shape of the pyramid is smoothed into a cone, but the carbon-carbon distances remain within the range of 1.42 ± 0.02 Å. That distance for the pentagon is 1.44 Å which is only about 1% longer than for the hexagons in graphite.

B. Electronic states

Self-consistent electronic states of the cluster are calculated using the density-functional method with the local-density approximation.¹⁶ The linear-combination-of-atomic-orbitals (LCAO) method is used. Radial wave functions of atoms are obtained by solving numerically the Schrödinger equation for atoms. Atomic orbitals used are 1s, 2s, and 2p orbitals for carbon atoms and 1s orbital for hydrogen atoms. C_{5v} symmetry is assumed in the calculations.

C. STM images

STM images are simulated using only the local density of states of the sample cluster.¹⁷ The tunneling current I at a bias voltage V and a tip position \mathbf{r} is expressed as

$$I \propto \int_{E_F}^{E_F+eV} \rho(\mathbf{r}, E) dE, \quad (2.1)$$

where

$$\rho(\mathbf{r}, E) = \sum_i |\Psi_i(\mathbf{r})|^2 \delta(E - E_i). \quad (2.2)$$

In the above, $\Psi_i(\mathbf{r})$ is the i th wave function of the cluster with an energy E_i . E_F is the Fermi energy.

In the present calculation, the δ function is replaced by a Lorentz function. This is because the conical protuberances observed in the experiment are actually not isolated clusters. Since tunneling current flows, they should be connected with bulk parts. This effect is taken into account by introducing the self-energy and the δ function is broadened into a Lorentz function. The energy width in the Lorentz function is chosen at 0.1 eV which is approximately the interval of the energy levels of the cluster.

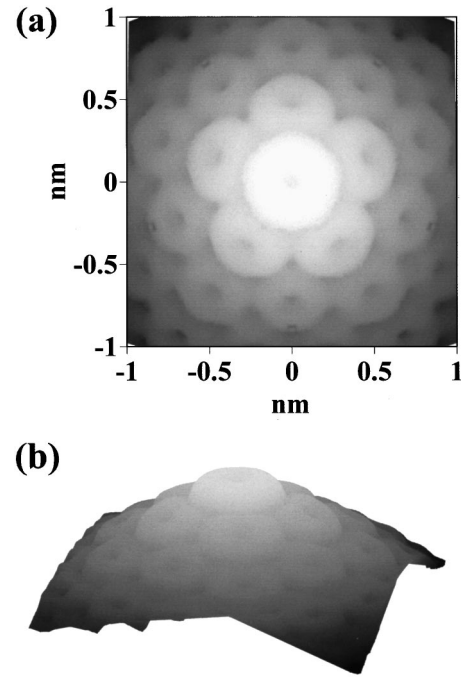


FIG. 2. Simulated STM images of the graphitic cone. The images are displayed in (a) grayscale and (b) three-dimensional view of the constant-current surface.

III. RESULT AND DISCUSSION

A. Simulated images

Figure 2 shows simulated STM images. The bias voltage is +50 mV. Here we define the bias voltage as the sample bias measured from the tip bias. The STM images are simulated in the constant-current mode. The fixed current is the value at the position of the tip 2.6 Å above a carbon atom of the pentagon along the symmetry axis of the cone. The scan plane is perpendicular to the symmetry axis.

In these images, we see not the honeycomb structure of the graphite lattice but a petal-like structure consisting of ring patterns. The sizes of the rings except for the center ring are approximately that of a hexagon in graphite. The ring patterns form a nearly $\sqrt{3} \times \sqrt{3}$ superstructure of the graphite lattice. The superstructure is also obtained for low negative bias voltages and fades away with increase of magnitude of the bias voltage. This means that the superstructure reflects special wave functions near the Fermi level. These features are in good agreement with the experiment.¹¹

The shapes of the rings are elliptically deformed. The center ring is about two times larger than the other rings and does not correspond to the atomic positions of the pentagon. These results, however, are apparent, because the surface of the graphitic cone tilts against the scan plane of Fig. 2. Figure 3(a) shows a STM image simulated for a scan plane tilted by θ , where $\cos \theta = 1/[\sqrt{3} \sin(\pi/5)]$. This tilted plane is almost parallel to the surface of a 1/5 part of the cluster. Closed circles show atomic positions of the cluster projected onto the scan plane.

In this figure, the ring patterns correspond exactly to the atomic positions of the graphitic cone. The elliptical deformation of the ring patterns in Fig. 2 is apparent due to the tilt. This is similar to the apparent distortion in nanotubes.¹⁸

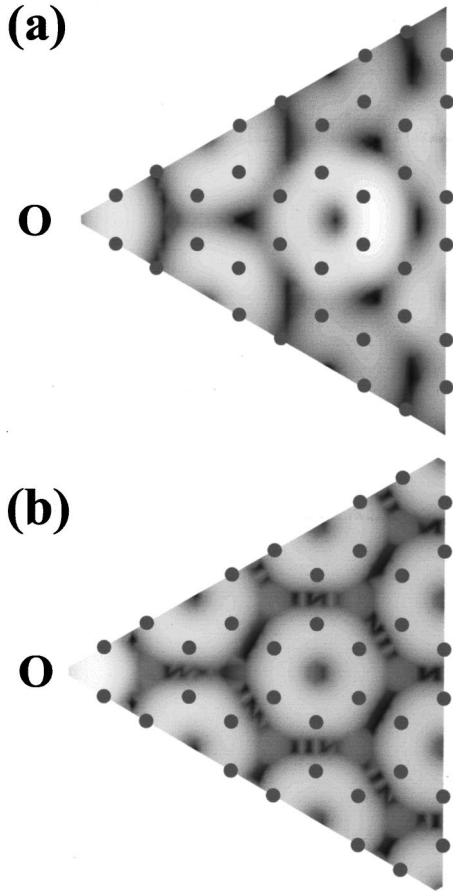


FIG. 3. Simulated STM images of the graphitic cone (a) based on density-functional calculations and (b) using the effective-mass theory. The scan plane is tilted almost parallel to the surface of the graphitic cone. Closed circles show the positions of carbon atoms projected onto the scan plane. The images show the $1/5$ part of the graphitic cone. The point O is the center of the pentagon.

The size of the center ring in Fig. 2 is apparently larger than that of the pentagon, because the directions of the π orbitals of the pentagon are not exactly perpendicular to the plane containing the pentagon atoms but tilt outward. Here “ π orbitals” means the atomic orbitals constituting wave functions near the Fermi level. Since the scan plane of the tip is far from the positions of the atoms, the pentagon in Fig. 2 is seen larger than actual size. The direction of the π orbital at each site is approximately perpendicular to the plane containing three nearest-neighbor atoms. Actually, a tight-binding calculation with only π orbitals reproduces well the image shown in Fig. 2, where the directions of the π orbitals are locally varied as stated above. In other words, this result means that information on the tip-sample distance is obtained from the apparent size of the pentagon.

B. Effective-mass theory

The origin of the ring patterns can be understood using effective-mass theory,¹³ which was originally used for the study of nanotube junctions. In the LCAO scheme with only the π orbitals, the wave function is expressed as

$$\Psi(\mathbf{r}) = \sum_{\mathbf{R}} C(\mathbf{R}) \phi(\mathbf{r} - \mathbf{R}), \quad (3.1)$$

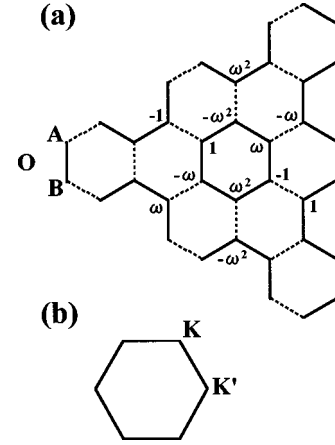


FIG. 4. (a) The factor $f(\mathbf{R})$ defined in Eqs. (3.3) and (3.4). The region shown is the same as those in Fig. 3. Dotted lines show antiphase bonds. A and B show the A and B sites, respectively. (b) The first Brillouin zone of two-dimensional graphite. The K and K' points are shown.

where $\phi(\mathbf{r})$ and \mathbf{R} are the π orbital and the position of the carbon atoms, respectively.

By applying the effective-mass theory to a graphite sheet with a pentagon defect, the coefficient for wave functions at the Fermi level is obtained as

$$C(\mathbf{R}) \propto f(\mathbf{R}) z^{(3m+2)/5}. \quad (3.2)$$

Details are shown in the Appendix. In the above, m is an integer and z is a complex number given by $z = R e^{i\theta}$, where R is the distance of the site \mathbf{R} from the center of the pentagon. θ is the azimuthal angle. $f(\mathbf{R})$ is given by

$$f(\mathbf{R}_A) = e^{i\mathbf{K} \cdot \mathbf{R}_A}, \quad (3.3)$$

for the A site and

$$f(\mathbf{R}_B) = e^{i\mathbf{K}' \cdot \mathbf{R}_B} (-1)^m \omega^2, \quad (3.4)$$

for the B site. In the above, $\omega = e^{i2\pi/3}$. \mathbf{K} and \mathbf{K}' are wave vectors at the K and K' points in the Brillouin zone of two-dimensional graphite. The A and B sites and the K and K' points are shown in Fig. 4. Since the complex conjugate of Eq. (3.2) is also a solution, $C(\mathbf{R})$ can be chosen real.

With increase of the absolute value of the exponent $|(3m+2)/5|$ in Eq. (3.2), the wave functions localize more strongly. Therefore, the solution with $m = -1$ contributes most to the electrical transport in STM. Figure 3(b) shows a STM image simulated using Eqs. (3.1)–(3.4) with $m = -1$ and its complex conjugate. In the simulation, we assume that $\phi(\mathbf{r})$ is proportional to $z e^{-\lambda r}$ for simplicity, where z is the coordinate perpendicular to the cone surface. The decay constant λ is 1.5 \AA^{-1} , which is determined by fitting to the $2p$ orbitals obtained in the density-functional calculation. The effective-mass theory qualitatively reproduces the image simulated based on the density-functional calculation shown in Fig. 3(a).

Figure 4 shows the factor $f(\mathbf{R})$ defined in Eqs. (3.3) and (3.4). This explains the $\sqrt{3} \times \sqrt{3}$ ring patterns. The factor is antiphase between neighboring atoms in neighboring rings, but it is not antiphase between atoms within each ring. Though the coefficient $C(\mathbf{R})$ is $f(\mathbf{R})$ multiplied by $z^{-1/5}$, the

z dependence is weak between neighboring atoms for large R and the patterns in the STM images are governed mainly by $f(\mathbf{R})$. It can also be shown by using the effective-mass theory that in the case of a heptagon defect the factor $f(\mathbf{R})$ of the most extended wave functions is the same as that shown in Fig. 4. Therefore, STM images similar to those around the pentagon defect are also expected around a heptagon defect. Furthermore, it can also be shown using the effective-mass theory that no superstructure appears around even-membered rings and only one type of superstructure different from the ring pattern is possible around a trigonal defect.

These $\sqrt{3} \times \sqrt{3}$ superstructures are different from those observed often around defects of flat graphite surfaces. The latter are caused by the scattering of extended Bloch waves at the K and K' points.¹² The wave functions of superstructures induced by topological defects are not extended but decay or grow with powers of the distance from the pentagon. This means that the size of the graphitic cones is an important factor for the superstructures to be observed. With increase of the size, the superstructure would be less visible. Furthermore, various types of patterns are observed in the superstructures of flat graphite surfaces with defects,¹⁹ because the amplitudes and relative phases of the waves at K and K' depend on details of the scattering potential of the defects. On the other hand, in the case of topological defects, the superstructures do not depend on the potential at the defects. Equations (3.3) and (3.4) show that there are only two types of patterns and the pattern experimentally observed is almost restricted to the ring pattern. This property is useful for identifying the observed structures with graphitic cones.

The present case is similar to screw dislocations in crystals.¹⁴ It was shown that the Schrödinger equation of an electron around a screw dislocation is equivalent to that in a vector potential, and phenomena similar to the Aharonov-Bohm (AB) effect are expected around screw dislocations. The pentagon defect in a graphite sheet plays the same role as screw dislocations and the superstructure is interpreted as an interference pattern in the AB effect, because the superstructure appears without any classical force and is essentially caused by the topological factor around the defect. In the case of the graphitic cones we observe the topological effect directly by STM.

IV. CONCLUSION

We presented theoretical STM images of a graphitic cone with a pentagon defect simulated based on density-functional calculations. The simulated images reproduce well the petal-like superstructure observed in experiment. The origin of the superstructure was clarified using the effective-mass theory. It was found that the superstructure in the graphitic cones is

induced by the topological defect and is qualitatively different from those often observed on flat graphite surfaces around defects.

ACKNOWLEDGMENTS

We thank K. Yokogawa for useful discussions and for showing us experimental data prior to publication. Numerical calculations were performed at supercomputers at the Institute of Molecular Science. This work was partially supported by a Grant-in-Aid from the Ministry of Education, Science, Sports and Culture, Japan.

APPENDIX

In this Appendix, we derive Eq. (3.2). Within the effective-mass approximation,¹³ the coefficient in wave functions near the Fermi level is expressed as

$$C(\mathbf{R}_A) = e^{i\mathbf{K} \cdot \mathbf{R}_A} F_A^K(\mathbf{R}_A) + e^{i\mathbf{K}' \cdot \mathbf{R}_A} F_A^{K'}(\mathbf{R}_A) \quad (\text{A1})$$

for the A site and

$$C(\mathbf{R}_B) = e^{i\mathbf{K} \cdot \mathbf{R}_B} F_B^K(\mathbf{R}_B) + e^{i\mathbf{K}' \cdot \mathbf{R}_B} F_B^{K'}(\mathbf{R}_B) \quad (\text{A2})$$

for the B site.

In the case of the pentagon defect, the envelope functions must satisfy the boundary conditions¹³

$$\begin{aligned} F_A^K[R(5\pi/3)\mathbf{r}] &= \omega^{-1} F_B^{K'}(\mathbf{r}), \\ F_B^K[R(5\pi/3)\mathbf{r}] &= -F_A^{K'}(\mathbf{r}), \\ F_A^{K'}[R(5\pi/3)\mathbf{r}] &= -\omega^{-1} F_B^K(\mathbf{r}), \\ F_B^{K'}[R(5\pi/3)\mathbf{r}] &= F_A^K(\mathbf{r}), \end{aligned} \quad (\text{A3})$$

where $R(5\pi/3)$ is a rotation operator by $5\pi/3$ around the center of the pentagon.

Since the envelope functions $F_A^K(\mathbf{r})$ and $F_B^{K'}(\mathbf{r})$ at the Fermi level are functions of only $z = x + iy$,¹³ a kind of solution satisfying the above boundary conditions is

$$\begin{aligned} F_A^K(\mathbf{r}) &= z^{(3m+2)/5}, \\ F_B^{K'}(\mathbf{r}) &= (-1)^m \omega^2 z^{(3m+2)/5}, \\ F_A^{K'}(\mathbf{r}) &= 0, \\ F_B^K(\mathbf{r}) &= 0, \end{aligned} \quad (\text{A4})$$

which is the solution shown in Eq. (3.2).

¹J. W. G. Wildöer, L. C. Venema, A. G. Rinzier, R. E. Smalley, and C. Dekker, *Nature (London)* **391**, 59 (1998).

²T. W. Odom, J.-L. Huang, P. Kim, and C. M. Lieber, *Nature (London)* **391**, 62 (1998).

³D. L. Carroll, P. Redlich, P. M. Ajayan, J. C. Charlier, X. Blase, A. De Vita, and R. Car, *Phys. Rev. Lett.* **78**, 2811 (1997).

⁴P. Kim, T. W. Odom, J.-L. Huang, and C. M. Lieber, *Phys. Rev. Lett.* **82**, 1225 (1999).

⁵R. Tamura and M. Tsukada, *Phys. Rev. B* **49**, 7697 (1994).

⁶R. Tamura and M. Tsukada, *Phys. Rev. B* **52**, 6015 (1995).

⁷R. Tamura, K. Akagi, M. Tsukada, S. Itoh, and S. Ihara, *Phys. Rev. B* **56**, 1404 (1997).

- ⁸S. Ihara, S. Itoh, K. Akagi, R. Tamura, and M. Tsukada, Phys. Rev. B **54**, 14 713 (1996).
- ⁹M. Ge and K. Sattler, Chem. Phys. Lett. **220**, 192 (1994).
- ¹⁰A. Krishnan, E. Dujardin, M. M. J. Treacy, J. Higdahl, S. Lynum, and T. W. Ebbesen, Nature (London) **388**, 451 (1997).
- ¹¹B. An, S. Fukuyama, K. Yokogawa, M. Yoshimura, M. Egashira, Y. Korai, and I. Mochida (unpublished).
- ¹²H. A. Mizes and J. S. Foster, Science **244**, 559 (1989).
- ¹³H. Matsumura and T. Ando, J. Phys. Soc. Jpn. **67**, 3542 (1998).
- ¹⁴K. Kawamura, Z. Phys. B **29**, 101 (1978).
- ¹⁵E. Burgos, E. Halac, and H. Bonadeo, Chem. Phys. Lett. **298**, 273 (1998).
- ¹⁶H. Adachi, M. Tsukada, and C. Satoko, J. Phys. Soc. Jpn. **45**, 875 (1978).
- ¹⁷J. Tersoff and D. R. Hamann, Phys. Rev. B **31**, 805 (1985).
- ¹⁸V. Meunier and P. Lambin, Phys. Rev. Lett. **81**, 5588 (1998).
- ¹⁹J. Xhie, K. Sattler, U. Müller, N. Venkateswaran, and G. Raina, Phys. Rev. B **43**, 8917 (1991).